Theory of far-infrared generation by optical mixing

J. R. Morris* and Y. R. Shen
Physics Department, University of California, Berkeley, California 94720
and Materials and Molecular Science Research Division, Lawrence Berkeley Laboratory and Department of Chemistry, University of California, Berkeley, California 94720
(Received 2 August 1976)

The theory of far-infrared generation by optical mixing of focused Gaussian beams is developed, taking into account the effects of diffraction, absorption, double refraction, and multiple and total reflections at the boundary surfaces. Results of numerical calculations are presented. It is shown that focusing of the pump beams appreciably enhances the far-infrared output despite the strong far-infrared diffraction. In a 1-cm-long crystal, the optimum focal-spot size is approximately equal to or smaller than the far-infrared wavelength for an output at frequency less than 100 cm^{-1}. Double refraction of the pump beams is relatively unimportant. Both far-infrared absorption and boundary reflections have major effects on the far-infrared output and its angular distribution. The former is often the factor which limits the output power. We show that a simple model treating the nonlinear polarization as a constant-$1/e$-radius Gaussian distribution of radiating dipoles is a good approximation to the problem. We also compare the results of our calculations with those for second-harmonic generation.

I. INTRODUCTION

Far-infrared generation by optical mixing has recently received increasing attention.[1] It has the potential of providing a coherent tunable far-infrared source which complements far-infrared molecular lasers. The most commonly used scheme is that of difference-frequency generation (DFG) by the mixing of two laser beams in a noncentrosymmetric crystal. With dye lasers,[2-3] Co_2 lasers,[4-16] or spin-flip Raman lasers[17-20] as the pump beams, DFG can provide a far-infrared source discretely or continuously tunable from 1 to 200 cm^{-1} or more. The output linewidth can easily be less than 0.1 cm^{-1} as determined by the pump laser linewidths. In most cases, the output is in pulses with pulsewidths between 10 nsec and 10 μsec, but cw operation has recently been achieved.

A serious limitation of far-infrared generation by optical mixing has been the attainable average power, although so far as spectral power per unit solid angle is concerned it is already better than a blackbody source at 5000 °K.[1] While focusing of the pump beams may increase the far-infrared output, it is not clear how tight the focusing can be before the detrimental effect of far-infrared diffraction sets in. No adequate theoretical calculation of nonlinear far-infrared generation with focusing and diffraction properly taken into account has been reported. Experimentally, on the other hand, a tight focusing geometry has so far been avoided. As a result, the full potential of nonlinear far-infrared generation has not been assessed.

In the literature, the plane-wave theory was often used to interpret the results of far-infrared generation experiments.[2,6,7,11,12,21-25] The theory assumes a single spatial Fourier component for each monochromatic wave so that the nonlinear process is characterized by a single phase-matching relation. However, when the pump beams are focused to a spot comparable in size to the far-infrared wavelength, far-infrared diffraction is important and the spatial Fourier components of the output extend over a large cone. Each Fourier component now has its own phase-matching relation with respect to the pump beams. Since it is not possible to phase match all the Fourier components simultaneously, focusing of the pump beams does not improve the far-infrared output power as much as the plane-wave theory predicts.

The plane-wave theory also assumes a single transmission coefficient for the far-infrared output across the boundary surface. Actually, with the far-infrared output extending over a large cone, the transmission coefficient is different for each Fourier component and falls to zero at the total reflection angle. Thus the real output can be considerably less than what the plane-wave theory predicts. Finally, the plane-wave theory often ignores the reduction in output power due to double refraction which can be significant for small spot sizes in crystalline media.

Improvement in the calculations of far-infrared generation by optical mixing has been achieved by Faries *et al.*[26] using the far-field diffraction theory for a distribution of oscillating dipoles induced by the pump beams.[26-28] They used an average transmission coefficient for the far-infrared output across the boundary and excluded the contribution from the totally reflected modes. The effect of double refraction was however ignored. As we shall see later, in the absence of double refraction, this approach in fact gives a remarkably good estimate of the far-infrared output.

In this paper we present a more rigorous calculation of far-infrared generation by optical mixing. It proceeds by first calculating separately each Fourier component of the output field and then evaluating the output power by summing over the Fourier components. The effects of focusing, absorption, phase matching, and double refraction can all be properly taken into account. For the sake of simplicity, the pump beams are assumed to be of single mode with Gaussian profiles. Our approach is essentially the same as that used by Bjorkholm[29] and by Kleinman *et al.*[30] for second-harmonic generation by focused beams.

The main difference between second-harmonic (or sum-frequency) generation in the visible or near infrared and difference-frequency generation in the far infrared is diffraction. Validity of the scalar Fresnel approximation for the pump beams guarantees its validity for the sum frequency but not for the difference frequency. Because of its much longer wavelength and hence stronger diffraction, the far-infrared output extends over a much broader cone. Thus the phase-matching condition varies much more appreciably among the output Fourier components in difference-frequency generation (DFG) than in sum-frequency generation (SFG). All the Fourier components can often be nearly simultaneously phase matched for SFG but not for DFG. An accurate description of DFG also requires knowledge of the difference-frequency transmission coefficients over a very broad output cone.

The body of the paper is organized into the following sections. Section II describes the theory of DFG by monochromatic Gaussian laser beams which is valid even when the pump focal spot size is smaller than a far-infrared wavelength. This theory is developed from a generalization of the nonlinear polarization used by Boyd and Kleinman[31] and by Faries.[28] Section III contains the results of numerical calculations obtained from this theory. First we present the results for the ideal case of no double refraction. Then we discuss briefly the reductions in attainable power due to far-infrared absorption and double refraction. Finally, in Sec. IV, we compare our results with the results of three other calculations: a simple plane-wave calculation, a far-field diffraction calculation assuming a constant-$1/e$-radius Gaussian distribution of induced dipoles, and the second-harmonic generation calculations of Boyd and Kleinman.[31]

II. THEORY

A. Nonlinear polarization

We assume that the pump beams are monochromatic with the Gaussian TEM_{00} mode. If focusing and diffraction of the pump beams are not too strong the focused pump fields in a slab medium can be written[28,31]

$$\vec{\mathrm{E}}_i(\vec{\mathrm{r}},t)=\frac{\mathcal{E}_i}{1+i\xi_i}\exp\left(\frac{(x-a_i-\zeta_i z)^2+y^2}{w_i^2(1+i\xi_i)}+ik_i z-\omega_i t\right) \tag{1}$$

for $0\le z\le l$, where the subindex i denotes the ith beam; w_i is the e^{-2} beam radius in the focal plane which is located at $z=z_{0i}$; the beam axis intersects the front surface of the medium at $x=a_i$ and $y=0$; the quantity ξ_i is defined by $\xi_i=2(z-z_{0i})/k_i w_i^2$ with $k_i=\omega_i n_i/c$, n_i being the refractive index; finally ζ_i is the walk-off angle given by $\zeta_i=\frac{1}{2}\sin(2\theta_i)n_i^2(n_{em,i}^{-2}-n_{o,i}^{-2})$ if the beam is an extraordinary ray propagating in a uniaxial medium along a direction at an angle θ with respect to the optical axis where $n_{o,i}$ and $n_{em,i}$ are, respectively, the ordinary and extraordinary refractive indices at $\theta=90°$. The derivation of Eq. (1) involves some approximations which can easily be justified as shown in Appendix A. In the following, to simplify the calculations in practical cases, we can assume that the largely overlapping pump beams are focused to the same spot size at the same point with $w_i\equiv w$, $\xi_i\equiv\xi$, and $z_{0i}\equiv z$. This is a good approximation when the refractive indices of the pump beams are not very different, as is true in all practical cases which have been investigated.

The pump fields now induce a nonlinear polarization at the far-infrared frequency in the medium. We consider here only the case of DFG in a uniaxial crystal as an example, although the formalism can be easily extended to more general cases of optical mixing. The nonlinear polarization at the difference frequency ω is then given by

$$\vec{\mathrm{P}}^{(2)}(\vec{\mathrm{r}},\omega)=\vec{\chi}^{(2)}(\omega=\omega_1-\omega_2):\vec{\mathrm{E}}_1(\vec{\mathrm{r}},\omega_1)\vec{\mathrm{E}}_2^{*}(\vec{\mathrm{r}},\omega_2), \tag{2}$$

where $\vec{\chi}^{(2)}$ is the second-order nonlinear susceptibility tensor. We assume that $\vec{\mathrm{E}}_1$ is an ordinary ray and $\vec{\mathrm{E}}_2$ is extraordinary. The nonlinear polarization $\vec{\mathrm{P}}^{(2)}(\vec{\mathrm{r}})$ can be readily found by substituting the expression of $\vec{\mathrm{E}}_i$ of Eq. (1) into Eq. (2). For convenience of solving the wave equation later, we are however interested in the transverse Fourier components of $\vec{\mathrm{P}}^{(2)}(\vec{\mathrm{r}})$. The transverse Fourier transform gives

$$\vec{\mathrm{P}}^{(2)}(\vec{\mathrm{k}}_T,z)=\frac{1}{2\pi}\int_{-\infty}^{\infty}dxdy\,\vec{\mathrm{P}}^{(2)}(\vec{\mathrm{r}})\exp(-ik_x x-ik_y y)$$

$$=\vec{\chi}^{(2)}:\vec{\mathcal{E}}_1\vec{\mathcal{E}}_2^{*}\tfrac{1}{4}w^2\exp\{i[(k_1-k_2^{*})z-k_x(a_1-\zeta z)/2]\}\exp\left(-\frac{(a_1-\zeta z)^2}{2w^2}-\frac{1}{8}k_T^2w^2(1+\xi^2)-\frac{1}{2}k_x(a_1-\zeta z)\xi\right), \tag{3}$$

where $\vec{k}_T = \hat{x}k_x + \hat{y}k_y$ and we set $a_2 = 0$ as part of a convenient choice of the origin. For economy of notation, we omit explicit mention of the argument ω.

B. Solution of wave equations

Far-infrared generation by optical mixing is described by the set of wave equations

$$[\nabla \times (\nabla \times) - (\omega^2/c^2)\vec{\epsilon}\cdot]\vec{E}(\vec{r},\omega) = 4\pi(\omega^2/c^2)\vec{P}^{NL}(\vec{r},\omega) \tag{4a}$$

and

$$\nabla\cdot[\vec{\epsilon}\cdot\vec{E}(\vec{r},\omega)] = -4\pi\nabla\cdot\vec{P}^{NL}(\vec{r},\omega)\,, \tag{4b}$$

where the nonlinear polarization P^{NL} acts as a driving source for the nonlinear process. For DFG in a uniaxial medium, $P^{NL} = P^{(2)}$ given by Eq. (2). Since the normal to the slab boundary planes is $\hat{z}$, the easiest method is to Fourier transform the x and y variables in Eq. (4) and to solve for each Fourier component $\vec{E}(\vec{k}_T, z)$ separately.[32] The corresponding source term for $\vec{E}(\vec{k}_T, z)$ is $4\pi(\omega^2/c^2)\vec{P}^{(2)}(\vec{k}_T, z)$ with $\vec{P}^{(2)}(\vec{k}_T, z)$ given by Eq. (3).

The general solution for $\vec{E}(\vec{k}_T, z)$ consists of two parts, the homogeneous solution and the particular solution, respectively. The homogeneous solution is well known. For ordinary and extraordinary polarizations, respectively, it can be written

$$\vec{E}^h_{o\pm}(\vec{k}_T, z) = \mathcal{E}_{o\pm}\hat{o}_\pm e^{ik_{o\pm,z}z}$$

and

$$\vec{E}^h_{e\pm}(\vec{k}_T, z) = \mathcal{E}_{e\pm}\hat{e}_\pm e^{ik_{e\pm,z}z}\,, \tag{5}$$

where the subindices "+" and "−" denote forward and backward propagating waves, respectively, with the same $\vec{k}_T$, and $k_{o\pm,z} = \pm[\omega n_o/c)^2 - k_T^2]^{1/2}$ with a similar expression for $k_{e\pm,z}$. To find the particular solution, let us first assume that the nonlinear slab is imbedded in a linear medium with an equal linear dielectric constant. Thus reflection and refraction at the crystal boundaries can be ignored. The boundary effects will be taken into account later. As shown in Appendix B, the particular solution for $E(\vec{k}_T, z)$ is then given by

$$\vec{E}^p(\vec{k}_T, z) = E^p_{o+}(\vec{k}_T, z)\hat{o}_+ + E^p_{o-}(\vec{k}_T, z)\hat{o}_- + E^p_{e+}(\vec{k}_T, z)\hat{e}_+ + E^p_{e-}(\vec{k}_T, z)\hat{e}_- - (4\pi n_e^2/n_o^2 n_{em}^2)\hat{z}P^{(2)}(\vec{k}_T, z)\,, \tag{6}$$

where n_{em} is the refractive index for an extraordinary ray propagating perpendicular to the optical axis,

$$E^p_{o+}(\vec{k}_T, z) = \frac{2\pi i\omega^2}{c^2 k_{oz}}\int_0^z \hat{o}_+\cdot\vec{P}^{(2)}(\vec{k}_T, z')e^{ik_{oz}(z-z')}dz'\,,$$

$$E^p_{o-}(\vec{k}_T, z) = \frac{2\pi i\omega^2}{c^2 k_{oz}}\int_z^l \hat{o}_-\cdot\vec{P}^{(2)}(\vec{k}_T, z')e^{-ik_{oz}(z-z')}dz'\,,$$

$$E^p_{e+}(\vec{k}_T, z) = \frac{2\pi i\omega^2}{c^2(k_{ez})_{\mathrm{eff},+}}\int_0^z \hat{e}_+\cdot\vec{P}^{(2)}(\vec{k}_T, z')e^{ik_{e+,z}(z-z')}dz'\,, \tag{7}$$

$$E^p_{e-}(\vec{k}_T, z) = \frac{2\pi i\omega^2}{c^2(k_{ez})_{\mathrm{eff},-}}\int_z^l \hat{e}_-\cdot\vec{P}^{(2)}(\vec{k}_T, z')e^{ik_{e-,z}(z-z')}dz'\,,$$

$$(k_{ez})_{\mathrm{eff},\pm} = \frac{(k_{e+,z} - k_{e-,z})n_{em}^2}{2n_e^2\{1 - [(n_o^2 - n_{em}^2)/n_o^2](\hat{c}\cdot\vec{k}_{e\pm})^2/k_o^2\}}\,.$$

$\hat{c}$ is the optical axis of the crystal. The last term in Eq. (6) is a longitudinal field which leads to optical rectification[33] when $\omega = \omega_1 - \omega_2 = 0$. It is, however, a nonradiating term and we shall neglect it in the following discussion.

The solution in Eqs. (6) and (7) appear in the form normally obtained for nonlinear optical processes in the slowly varying envelope approximation. However, no such approximation has been made. As shown in Appendix B, Eq. (6) together with Eq. (7) is an exact solution of Eq. (4) with $\vec{P}^{(2)}(\vec{k}_T, z)$ as the source term. The field $\vec{E}^p(\vec{k}_T, z)$ in the medium does not have a slowly varying amplitude since $\partial^2|\vec{E}^p(\vec{k}_T, z)|/\partial z^2$ is not negligible in comparison with $2k\partial|\vec{E}^p(\vec{k}_T, z)|/\partial z$. In fact, the slowly varying envelope approximation is equivalent to assuming for each polarization a wave propagating in one direction only.

As a check, we can use Eqs. (6) and (7) to derive the solution for the special case of optical mixing at an infinite boundary surface discussed by Bloembergen.[34] We have $k_y = 0$, $l \to \infty$, and $\vec{P}^{(2)}(\vec{k}_T, z) = P_0\hat{y}e^{ik_{sz}z}$ in the medium. Equation (7) gives for the reflected output

$$\vec{E}^p_r = -\frac{2\pi\omega^2}{c^2 k_{oz}(k_{oz} + k_{sz})}\hat{y}P_0 e^{-ik_{oz}z} \text{ for } z < 0\,, \tag{8a}$$

and for the transmitted output

$$\vec{E}^p_t = \frac{2\pi\omega^2}{c^2 k_{oz}}\hat{y}P_0\left(\frac{2k_{oz}}{k_s^2 - k_o^2}e^{ik_{sz}z} - \frac{1}{k_{sz} - k_{oz}}e^{ik_{oz}z}\right) \text{ for } z > 0\,. \tag{8b}$$

The above solution is, however, only true for the case with no reflection at the boundary, but the boundary effects can be easily incorporated by taking into account the linear reflection of $\vec{E}^p_r$ at the boundary surface. The complete solution for the problem with a crystal-vacuum plane boundary is then given by

$$\vec{E}^p_R = \frac{2k_{oz}}{k_{oz} + k_z}\vec{E}^p_r(z=0)e^{-ik_z z} \text{ for } z < 0\,,$$
$$\vec{E}^p_T = \vec{E}^p_t - \frac{k_z - k_{oz}}{k_z + k_{oz}}\vec{E}^p_r(z=0)e^{ik_o z} \text{ for } z > 0\,, \tag{9}$$

where $k_z=[(\omega/c)^2-k_x^2]^{1/2}$. Substitution of the expressions for $\vec{E}_r^{\,p}$ and $\vec{E}_t^{\,p}$ in Eq. (8) into Eq. (9) yields results identical to those derived by Bloembergen.[34]

The above example suggests that the boundary effects can indeed be taken care of separately. In Sec. IIC we shall use the same procedure to take into account the boundary conditions of optical mixing in a slab medium. Then, with the expression of $\vec{P}^{(2)}(\vec{k}_T,z)$ in Eq. (3), we can calculate from Eqs. (5)–(7) and the appropriate boundary conditions the Fourier component $\vec{E}(\vec{k}_T,z)$ of the DFG output and hence the difference-frequency field $\vec{E}(\vec{r})$ in space. In many cases, only one of the four waves in Eq. (7) is nearly phase matched. When this happens, we need to retain only the phase-matched component in a good approximate calculation.

C. Boundary effects

We have seen in Sec. II B how we can take into account the boundary effects of a crystal-vacuum interface by simply incorporating linear reflection and transmission of the waves at the boundary into the solution. We now discuss the boundary effects of the more general case of a slab crystalline medium. We can consider $\vec{E}_+^{\,P}$ in Eq. (6) as forward propagating waves starting from $z=0$ in the medium and subsequently undergoing multiple partial reflections at the two slab surfaces. Similarly, we consider $\vec{E}_-^{\,p}$ (6) as backward propagating waves starting from $z=l$ in the medium. Thus the field outside the slab is given by the sum of $\vec{E}_+^{\,p}$ and $\vec{E}_-^{\,p}$ weighted, respectively, by appropriate Fabry-Perot factors due to multiple reflections and transmissions. To find the Fabry-Perot factors, we first calculate the transmission and reflection matrices for ordinary and extraordinary waves at a single-crystal vacuum boundary surface, and then find the overall transmission and reflection matrices of the slab for the two waves by summing over multiple transmissions and reflections at the slab surfaces.

Consider first the case defined in Fig. 1(a). The incident monochromatic plane wave $\vec{E}_{i+}(\vec{k}_T)=E_{i+}^{\parallel}\hat{\parallel}_+ + E_{i+}^{\perp}\hat{\perp}$ and the reflected plane wave $\vec{E}_{r-}(\vec{k}_T)=E_{r-}^{\parallel}\hat{\parallel}_- + E_{r-}^{\perp}\hat{\perp}$ are related to the refracted ordinary and extraordinary waves $\vec{E}_{o+}(\vec{k}_T)$ and $E_{e+}(\vec{k}_T)$, respectively, by the matrix relations[35]

$$\begin{pmatrix}E_{i+}^{\perp}\\E_{i+}^{\parallel}\end{pmatrix}=\vec{\mathrm{A}}_+\begin{pmatrix}E_{o+}\\E_{e+}\end{pmatrix},\qquad \begin{pmatrix}E_{r-}^{\perp}\\E_{r-}^{\parallel}\end{pmatrix}=\vec{\mathrm{B}}_+\begin{pmatrix}E_{o+}\\E_{e+}\end{pmatrix},\tag{10}$$

where

$$\vec{\mathrm{A}}_\pm\equiv\begin{pmatrix}\alpha_0^\pm/(1+r_0^\perp) & \alpha_e^\pm/(1+r_{e\pm}^\perp)\\ \beta_0^\pm k_0/(1+r_0^\parallel)k & \beta_e^\pm k_e/(1+r_{e\pm}^\parallel)k\end{pmatrix},$$

$$\vec{\mathrm{B}}_\pm\equiv\begin{pmatrix}\alpha_0^\pm r_0^\perp/(1+r_0^\perp) & \alpha_e^\pm r_{e\pm}^\perp/(1+r_{e\pm}^\perp)\\ \beta_0^\pm r_0^\parallel k_0/(1+r_0^\parallel)k & \beta_e^\pm r_{e\pm}^\parallel k_e/(1+r_{e\pm}^\parallel)k\end{pmatrix},$$

$$r_0^\perp\equiv(k_z-k_{oz})/(k_z+k_{oz}),$$

$$r_0^\parallel\equiv(k_0^2k_z-k^2k_{oz})/(k_0^2kz+k^2k_{oz}),$$

$$r_{e\pm}^\perp\equiv(-k_{ez}^\pm\pm k_z)/(k_{ez}^\pm\pm k_z),$$

$$r_{e\pm}^\parallel\equiv(-k^2\gamma_e^\pm\pm k_zk_e^\pm\beta_e^\pm)/(k^2\gamma_e^\pm\pm k_zk_e^\pm\beta_e^\pm),$$

$$\alpha_0^\pm\equiv\hat{o}_\pm\cdot(\hat{z}\times\hat{k}_T),\quad \beta_0^\pm\equiv\hat{o}_\pm\cdot[(\hat{z}\times\hat{k}_T)\times\hat{k}_0^\pm],$$

$$\alpha_e^\pm\equiv\hat{e}_\pm\cdot(\hat{z}\times\hat{k}_T),\quad \beta_e^\pm\equiv\hat{e}_\pm\cdot[(\hat{z}\times\hat{k}_T)\times\hat{k}_e^\pm],$$

$$\gamma_e^\pm\equiv\hat{e}_\pm\cdot\hat{k}_T.$$

With subindex "–" applied to the case of Fig. 1(b) with

$$\begin{pmatrix}E_{i-}^{\perp}\\E_{i-}^{\parallel}\end{pmatrix}=\vec{\mathrm{A}}_-\begin{pmatrix}E_{o-}\\E_{e-}\end{pmatrix},\quad \begin{pmatrix}E_{r+}^{\perp}\\E_{r+}^{\parallel}\end{pmatrix}=\vec{\mathrm{B}}_-\begin{pmatrix}E_{o-}\\E_{e-}\end{pmatrix}.$$

We next consider transmission and reflection of ordinary and extraordinary waves incident from the crystal side onto the boundary surface as described by diagram a in Fig. 2. Clearly, diagram a is equivalent to the sum of diagram b and diagram c, and diagrams b and c are identical to those in Figs. 1(a) and 1(c), respectively. We therefore have

$$\vec{E}_{t-}=\vec{E}'_{t-}+\vec{E}''_{t-}=\vec{\mathrm{T}}_-\begin{pmatrix}E_{o-}\\E_{e-}\end{pmatrix}$$

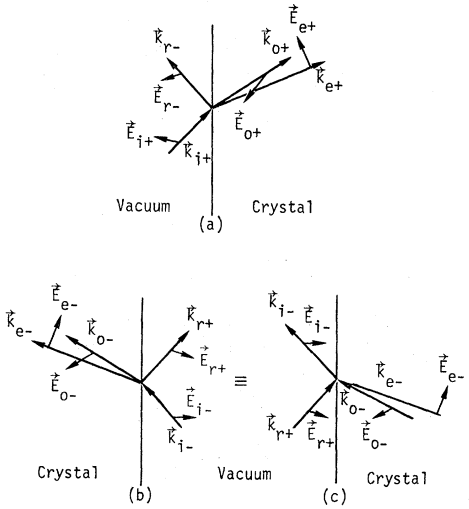

FIG. 1. Wave-vector diagram for reflection of a plane-wave incident from the vacuum side on the plane interface between vacuum and uniaxial crystal half-spaces: (a) crystal fills the right half-space, (b) crystal fills the left half-space, and (c) an equivalent diagram with the crystal on the right.

and

$$\begin{pmatrix} E_{o+} \\ E_{e+} \end{pmatrix} = \vec{\vec{R}}_- \begin{pmatrix} E_{o-} \\ E_{e-} \end{pmatrix}, \tag{11}$$

where

$$\vec{\vec{T}}_\pm = \vec{\vec{A}}_\pm - \vec{\vec{B}}_\mp \vec{\vec{A}}_\mp^{-1} \vec{\vec{B}}_\pm ,$$

$$\vec{\vec{R}}_\pm = -\vec{\vec{A}}_\mp^{-1} \vec{\vec{B}}_\pm ;$$

the subindices "+" and "−" now refer to cases where the crystalline medium occupies the left half-space and the right half-space, respectively.

We can now use the results in Eq. (11) to calculate the effect of multiple transmissions and reflections at the boundaries of a crystal slab. In particular, we are interested in finding the forward and backward propagating far-infrared waves outside the slab created by optical mixing inside the slab. As we mentioned earlier, we can imagine that optical mixing generates waves $\vec{E}_+^{\,p}$ starting at $z=0$ and $\vec{E}_-^{\,p}$ starting at $z=l$ and in getting out of the slab, these waves undergo multiple transmissions and reflections. Therefore for the generated field outside the slab, we readily find for $z=l$

$$\vec{E}_{T+} = \vec{\vec{T}}_+ \vec{\vec{F}}_+ \left[\begin{pmatrix} E_{o+}(l) \\ E_{e+}(l) \end{pmatrix} + \vec{\vec{P}}_+ \vec{\vec{R}}_- \begin{pmatrix} E_{o-}(0) \\ E_{e-}(0) \end{pmatrix} \right], \tag{12a}$$

and for $z<0$

$$\vec{E}_{T-} = \vec{\vec{T}}_- \vec{\vec{F}}_- \left[\begin{pmatrix} E_{o-}(0) \\ E_{e-}(0) \end{pmatrix} + \vec{\vec{P}}_- \vec{\vec{R}}_+ \begin{pmatrix} E_{o+}(l) \\ E_{e+}(l) \end{pmatrix} \right], \tag{12b}$$

where

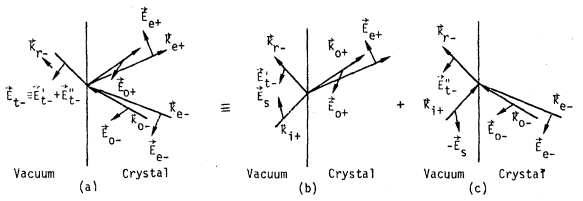

FIG. 2. Wave-vector diagrams showing (a) boundary transmission and reflection of ordinary and extraordinary waves and its decomposition into (b) and (c) which describe two simpler cases of linear transmission and reflection of waves at an interface.

$$\vec{\vec{P}}_\pm = \begin{pmatrix} \exp(ik_{o2}l) & \\ & \exp(\pm ik_{e2}^{\pm} l) \end{pmatrix}$$

and

$$\vec{\vec{F}}_\pm = (\vec{\vec{1}} - \vec{\vec{P}}_\pm \vec{\vec{R}}_\mp \vec{\vec{P}} \vec{\vec{R}}_\pm)^{-1} = \sum_{n=0}^{\infty} (\vec{\vec{P}}_\pm \vec{\vec{R}}_\mp \vec{\vec{P}}_\mp \vec{\vec{R}}_\pm)^n . \tag{13}$$

Because of the generalized Fabry-Perot factor $\vec{\vec{F}}_\pm$, the output fields $\vec{E}_{T\pm}$ can be rapidly varying functions of $\vec{k}_T$, ω, and l. In some cases, however, when the pump laser beams have fairly broad linewidths or the crystal slab is wedged or not sufficiently well polished, it is more appropriate to find an average Fabry-Perot factor or the average output by averaging over one Fabry-Perot period. For example, in the nearly isotropic case, we find from Eq. (12) after some manipulation,

$$\langle |\vec{E}_{T+}|^2 \rangle \propto \langle (\vec{\vec{T}}_+ \vec{\vec{F}}_+)^\dagger (\vec{\vec{T}}_+ \vec{\vec{F}}_+) \rangle = \begin{pmatrix} \alpha^{+*} & \beta^+ \\ \beta^+ & -\alpha^{+*} \end{pmatrix} \begin{pmatrix} \dfrac{|1-r_\perp|^2}{1-|r_\perp|^4 \exp(-\gamma l)} & 0 \\ 0 & \dfrac{|(1-r_\parallel)n|^2}{1-|r_\parallel|^4 \exp(-\gamma l)} \end{pmatrix} \begin{pmatrix} \alpha^+ & \beta^+ \\ \beta^+ & -\alpha^+ \end{pmatrix}, \tag{14}$$

where γ is the attenuation constant along $\hat{z}$.

D. Far-infrared output power and its far-field angular distribution

The total far-infrared power outputs from the slab in the forward and backward directions are

$$\mathcal{P}_\pm = \frac{c}{2\pi} \int dx\, dy\, (\hat{z} \cdot \hat{\Omega}) \left| \vec{E}_{T\pm}(x,y) \right|^2 \tag{15}$$

evaluated at large z. By Parseval's theorem, this can be written as

$$\mathcal{P}_\pm = \frac{c}{2\pi} \int_{k_x^2 + k_y^2 \le k^2} dk_x\, dk_y\, (\hat{z} \cdot \hat{k}^\pm) \left| \vec{E}_{T\pm}(\vec{k}_T) \right|^2 , \tag{16}$$

where $\vec{E}_{T\pm}(\vec{k}_T)$ is given by Eq. (12).

In most practical cases, we are also interested in the far-field angular distribution of the output power. As shown in the Appendix of Miyamoto and Wolf,[36] it has the expression

$$\frac{d\mathcal{P}_\pm(\theta,\phi)}{d\Omega} = \frac{c}{2\pi} \cos^2\theta \left| \vec{E}_{T\pm}\left(\vec{k}_T = \frac{\omega}{c} \sin\theta (\hat{x}\cos\phi + \hat{y}\sin\phi) \right) \right|^2 . \tag{17}$$

III. RESULTS OF NUMERICAL CALCULATIONS

In this section we shall present numerical calculations of far-infrared generation by difference-frequency mixing using the equations given in the previous section. We choose somewhat arbitrarily the following values for the characteristic parame-

ters of the nonlinear crystal: $n_o = 2$, $n(\omega) = 4$, and $\chi^{(2)} = 1.87 \times 10^{-6}$ esu. The two nearly overlapped pump beams, one ordinary and one extraordinary, are assumed to have the same focal spot in the crystal with both beams always along the normal to the slab. The question we propose to answer is how various quantities such as phase mismatch, focusing, beam walkoff, and absorption affect the far-infrared output at different frequencies.

A. Far-infrared generation in the absence of absorption and optical walkoff

We assume in this case that the optical axis of the crystal is in the plane of the slab along $\hat{x}$. The two pump beams, one ordinary and one extraordinary, propagate along the normal to the slab $\hat{z}$ with essentially no walkoff, the nonlinear polarization $\vec{P}^{NL}$ is along $\hat{y}$, and the common focal spot of the two pump beams is at the center of the slab. We also assume that the extraordinary refractive index n_{em} of the pump beam can be varied by external means such as temperature in order to adjust the amount of phase mismatch in DFG and that only the ordinary far-infrared waves in the forward direction can be nearly phase matched. Since the phase mismatch is different for different Fourier components $\vec{E}(\vec{k}_T, \omega)$ of the far-infrared output, we define an axial phase mismatch $\Delta k_a = k_1(\omega_1) - k_2(\omega_2) - k_o(\omega)$ to describe the overall phase-matching condition.

Figure 3 shows the far-field angular distribution of the far-infrared output $d\mathcal{P}(\theta)/d\Omega$ vs θ, at 100 cm^{-1} calculated from Eq. (17). In the calculation the slab has a thickness of 1 cm, the focal spot size is $w = 25$ μm, and the axial phase mismatch corresponds to $\Delta k_a = -5.1$ cm^{-1}. Since the far-infrared output is approximately symmetric about $\hat{z}$ [i.e., nearly independent of the azimuth angle $\phi = \tan^{-1}(k_y/k_x)$], Fig. 3 actually shows a distribution in the form of a hollow cone. The radiation peaks at the angle

$$\theta_m = \sin^{-1}\{n_o^2(\omega) - [n_o(\omega) + \Delta k_a c/\omega]^2\}^{1/2}$$

at which phase matching

$$\Delta k_z = k_1 - k_2 - k_{oz}(\omega) = 0$$

occurs. The secondary maxima of the phase-matching curve can also be seen. They become more pronounced for shorter far-infrared wavelengths as the effect of diffraction becomes less important. From the expression of θ_m, it is seen that if $\Delta k_a = 0$, then $\theta_m = 0$ and the far-infrared output appears as a narrow solid cone along the z axis. If $\Delta k_a > 0$, then there is no solution for θ_m and the far-infrared output is strongly suppressed by phase mismatch; the angular distribution may show a weak central peak at $\theta = 0$ and some secondary maxima at finite θ. For negative Δk_a, the phase-matched peak shifts to larger θ_m until $\theta_m = \frac{1}{2}\pi$; then because of total reflection at the surface, the far-infrared radiation in the phase-matched direction can no longer get out of the slab and the output peak at $\theta = \frac{1}{2}\pi$ drops quickly.

The total far-infrared power output $\mathcal{P}$ vs Δk_a is shown in Fig. 4 with the same set of parameters used for Fig. 3. The curve has a maximum around $\Delta k_a = -5.1$ cm^{-1} corresponding to the full development of the hollow phase-matched cone in Fig. 3. The steep rise of the curve at $\Delta k_a \sim 0$ cm^{-1} is due to the initial appearance of the phase-matched

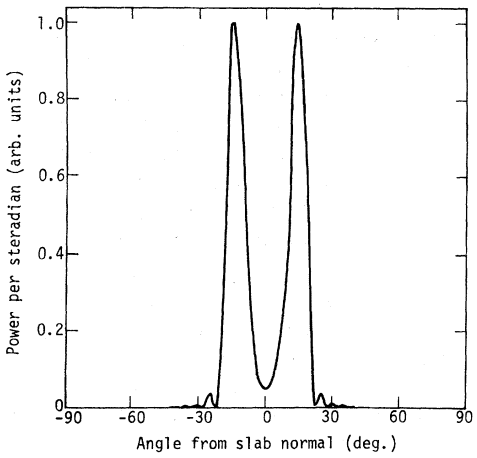

FIG. 3. Angular distribution of far-infrared power output at $\omega = 100$ cm^{-1} with the axial phase mismatch at its optimum value $\Delta k_a \simeq -5.1$ cm^{-1}, a near optimum focal spot radius $w = 25$ μm, a zero walkoff angle $\zeta = 0$, and a crystal length $l = 1$ cm.

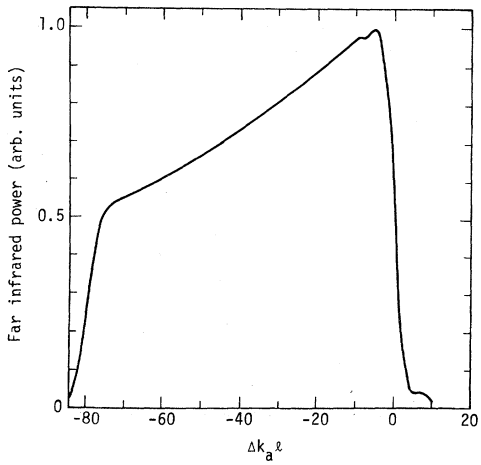

FIG. 4. Far-infrared power output at $\omega = 100$ cm^{-1} as a function of $\Delta k_a l$, assuming $\alpha = 0$, $\zeta = 0$, $w = 25$ μm, and $l = 1$ cm.

cone. The gradual decrease between $\Delta k_a \approx -10$ cm^{-1} and -75 cm^{-1} is due to the combined effects of decrease of the far-infrared transmission coefficients and decrease of the effective $P^{(2)}$ for the generation of ordinary far-infrared waves around the phase-matched direction. The steep drop after $\Delta k_a \approx -75$ cm^{-1} is due to total reflection of an increasing portion of those far-infrared waves generated near phase matching.

If the far-infrared wavelength λ inside the crystal becomes much smaller than the focal spot size w, the variation of far-infrared output versus phase mismatch Δk_a appears more like the usual phase-matching function $(\sin^2 x)/x^2$ for the ideal plane-wave case. An example is shown in Fig. 5 for the case of $\lambda = \frac{1}{8}w$. Because of the smaller λ/w ratio, the off-axis Fourier components of the far-infrared become relatively less important, and hence the output drops more rapidly with increase of Δk_a. The curve in Fig. 5 is, however, still noticeably asymmetric and its peak occurs at $\Delta k_a = -2$ cm^{-1} rather than $\Delta k_a = 0$. As the ratio of λ/w decreases further, the effect of far-infrared diffraction becomes even smaller; the phase-matching curve $\mathcal{P}$ vs Δk_a then develops more clearly defined secondary peaks and approaches the symmetric form $\sin^2(\Delta k_a l/2)/(\Delta k_a l/2)^2$.

The focusing geometry of the Gaussian pump beams is completely characterized by the focal spot size w. In order to see how the far-infrared output varies with focusing, we calculate the $\zeta = 0$ curve in Fig. 6 which shows the maximum of $\mathcal{P}(\Delta k_a)$ as a function of w. Because of the higher pump intensity resulting from tighter focusing, the far-infrared output increases sharply with decrease of w. However, it reaches a maximum at $w = 13$ μm as the corresponding reduction of the

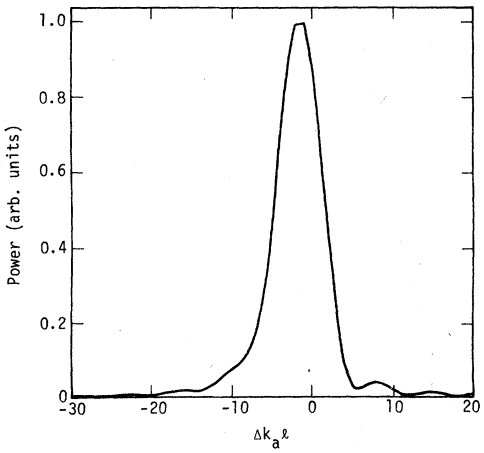

FIG. 5. Far-infrared power output at $\omega = 100$ cm^{-1} as a function of $\Delta k_a l$ assuming $\alpha = 0$, $\zeta = 0$, $w = 0.2$ mm, and $l = 1$ cm.

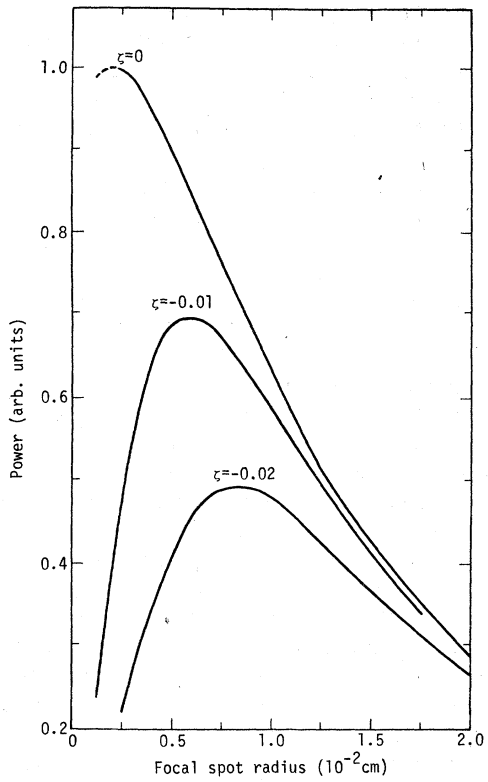

FIG. 6. Far-infrared power output at $\omega = 100$ cm^{-1} as a function of the focal spot radius w for various walkoff angles ζ, $\alpha = 0$, and $l = 1$ cm. The calculation was done by always adjusting the axial phase mismatch Δk_a to its optimum value for maximum power output.

longitudinal focal dimension takes its toll. It is interesting to note that in the model of collimated Gaussian pump beams with a radius w and with $w^2|E_1 E_2| = \text{constant}$, $\mathcal{P}$ vs w has no maximum. This is because when $k_T w \ll 1$ for all significant far-infrared Fourier components, $P^{(2)}(\vec{k}_T, z)$ in Eq. (3) becomes independent of k_T and w.

While Figs. 3–6 are for $\omega = 100$ cm^{-1}, Figs. 7–9 show results of similar calculation for $\omega = 10$ cm^{-1}. The far-field angular distribution of the output is given in Fig. 7 for two values of the azimuth angle $\phi = \tan^{-1}(k_y/k_x) = 0$ and $\frac{1}{2}\pi$. In this case, because $\lambda/w = 10$ is large, far-infrared diffraction is more important; phase matching occurs around $\theta = \frac{1}{4}\pi$ and the phase-matched peak is very broad. As a result, the output asymmetry with respect to ϕ shows up because at relatively large θ, the transmission coefficient for the ordinary far-infrared wave across the slab boundaries is different for different ϕ. For $\phi = 0$ the wave is linearly polarized perpendicular to the plane of incidence, while for $\phi = \frac{1}{2}\pi$ the wave is linearly polarized in the plane of incidence. The latter case has a Brewster angle at $\theta = 76°$.

Figure 8 shows the total far-infrared output at $\omega = 10\ \text{cm}^{-1}$ as a function of the axial phase mismatch Δk_a. The curve again resembles the well-known phase-matching curve $(\sin^2 x)/x^2$ for the plane-wave case except that its maximum is at $\Delta k_a = -4\ \text{cm}^{-1}$ instead of $\Delta k_a = 0$ and it has no well-defined nodes. However, this resemblance does not occur because diffraction is unimportant. It occurs because when the far-infrared wavelength is sufficiently long, then all the far-infrared Fourier components $\vec{E}(\vec{k}_T, z)$ have roughly the same $\Delta k_z l \approx \Delta k_a l$; in other words, if $\Delta k_a l = 0$, then all the far-infrared Fourier components are nearly phase matched. The small difference of $\Delta k_z l$ among the Fourier components, however, broadens the phase-matching peak and obscures the fine structure.

The $\zeta = 0$ curve in Fig. 9 describes the peak value of $\mathcal{P}(\Delta k_a)$ at $\omega = 10\ \text{cm}^{-1}$ as a function of the focal spot size w. We notice that in the range of our calculation, this maximum output power $\mathcal{P}_{\max}(\Delta k_a)$ always increases with decrease of w. In this case, $k_T w$ becomes so much smaller than 1 at small w that the nonlinear polarization $\vec{P}^{(2)}(\vec{k}_T)$ approaches a constant independent of k_T, w, and z in spite of the factor $(1+\xi^2)$ in the exponential function in Eq. (3). Consequently, the $\zeta = 0$ curve of Fig. 9 flattens out at small w. Eventually, for even smaller w, we should expect the curve to go through a maximum like the $\zeta = 0$ curve in Fig. 6 for $\omega = 100\ \text{cm}^{-1}$.

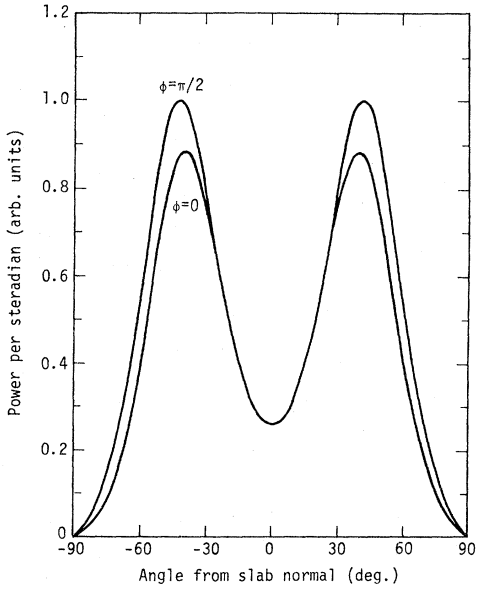

FIG. 7. Angular distribution of far-infrared power output at $\omega = 10\ \text{cm}^{-1}$ for $\Delta k_a = -4.0\ \text{cm}^{-1}$, $w = 25\ \mu\text{m}$, $\zeta = 0$, $\alpha = 0$, and $l = 1$ cm. The azimuth ϕ is defined by $\phi = \tan^{-1}(y/x)$.

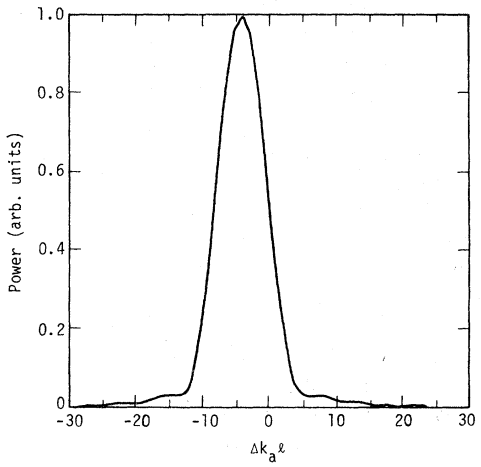

FIG. 8. Far-infrared power output at $\omega = 10\ \text{cm}^{-1}$ as a function of $\Delta k_a l$ assuming $\alpha = 0$, $\zeta = 0$, $w = 25\mu\text{m}$, and $l = 1$ cm.

B. Far-infrared generation with a finite walkoff angle between the pump beams

We now consider the effect of optical walkoff on far-infrared generation. We still assume that the pump beams propagate normal to the slab and absorption is negligible, but the orientation of the optical $\hat{c}$ axis of the crystal is now varied in the $\hat{x}-\hat{z}$ plane in order to vary the walkoff angle ζ. The primary effect of optical walkoff is that it limits the effective interaction length of the beams.

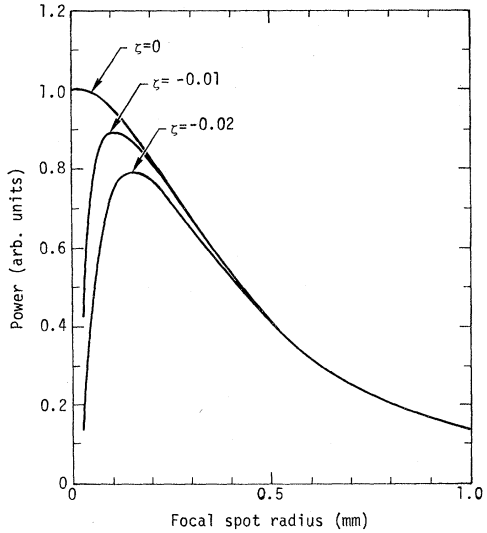

FIG. 9. Far-infrared power output at $\omega = 10\ \text{cm}^{-1}$ as a function of the focal spot radius w for various walkoff angles ζ, $\alpha = 0$, and $l = 1$ cm. The axial phase mismatch was always adjusted to its optimum value in the calculation.

When ζ is much larger than the divergence angle of the pump beams, the two pump beams overlap in the focal region only over a distance of $2w/|\zeta|$; most of the far-infrared radiation is generated from this overlapping region. As $|\zeta|$ increases, the effective interaction length decreases, and hence the phase-matching peak in the far-field angular distribution becomes weaker and broader, as shown in Fig. 10 for $\omega = 10$ cm^{-1}. For smaller focal spot sizes w, the walkoff effect is stronger. This gives rise to a lower maximum at a larger w for the $\zeta \neq 0$ curves in Figs. 6 and 9.

The far-infrared output should in general consist of both ordinary and extraordinary waves. We have so far assumed that the e wave is strongly phase mismatched and can be neglected. This is true for $\theta_c = \cos^{-1}(\hat{c} \cdot \hat{z})$ larger than the total reflection angle θ_R. However, when $\hat{c}$ approaches $\hat{z}$ or θ_c approaches zero, the phase mismatch of the e wave is greatly reduced and the e-wave output becomes non-negligible. For $\theta \approx 0$ we have the nearly degenerate case where the e wave and the o wave contribute almost equally to the far-infrared output.

There are two other less important effects of optical walkoff on far-infrared generation. First, the $\exp(ik_x\zeta z/2)$ term in Eq. (3) contributes to the phase-matching relation, which now becomes $\Delta k_z = k_1 - k_2 + k_x\zeta - k_z = 0$. This term shifts the center of the phase-matching cone in Figs. 3, 7, and 10 from $k_x = 0$ to $k_x = \frac{1}{2}\zeta(\Delta k_a + n_o\omega/c)$. Since for $\phi = 0$, the far-infrared transmission coefficient for o waves at the boundary falls off monotonically with increase of θ, this increases the phase-matched output for $k_x > 0$ and decreases that for $k_x < 0$. Second, as seen from Eq. (3), the maximum of $|\vec{P}^{(2)}(\vec{k}_T, z)|$ is shifted from $k_x = k_y = 0$ to $k_x = k_1\zeta\xi^2/(1+\xi^2)$ and $k_y = 0$; its effect on the far-field angular distribution is just the opposite of that due to the shift of the phase-matching cone. Depending on the situation, one effect may dominate over the other. They are responsible for the slight asymmetry of the $\zeta = 0$ curves in Fig. 10. The phase-matching effect is more important for the $\zeta = -0.01$ case while the $|P^{(2)}(k_T)|$ effect is more important for the $\zeta = -0.02$ case. For shorter crystals ($l \lesssim 0.5$ cm), the phase-matching effect is more important.

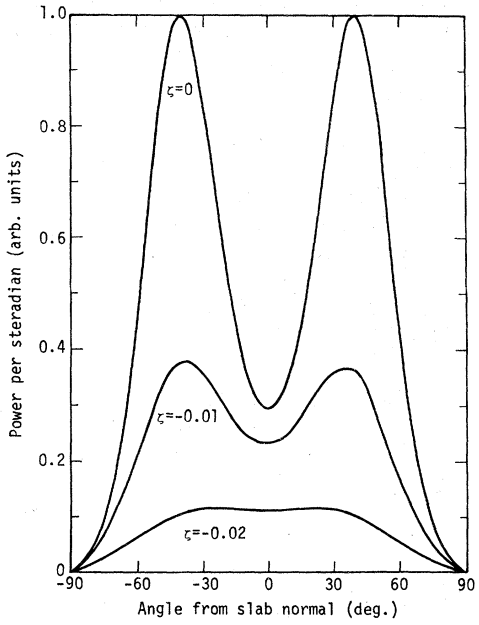

FIG. 10. Angular distribution of the far-infrared power output at $\omega = 10$ cm^{-1} for various walkoff angles ζ assuming $w = 25\ \mu$m, $\alpha = 0$, $l = 1$ cm, and the optimum value of $\Delta k_a(\zeta)$. All curves were computed in the $\phi = 0$ plane.

C. Effects of linear absorption on far-infrared generation.

In practice, nonlinear far-infrared generation in crystals is always limited by far-infrared absorption. This is the main reason why far-infrared DFG in solids has in most cases been restricted to the range between 1 and 200 cm^{-1}. Roughly speaking, with an absorption coefficient γ, the effective length of the crystal for DFG cannot be much more than $2/\gamma$.

Figure 11 shows how the far-infrared output from a 1-cm slab decreases as a function of the far-infrared absorption coefficient γ for $\omega = 10$ and 100 cm^{-1}. In the calculation, the focal spot size was chosen as $w = 25\ \mu$m and the location of the focal spot was at the center of the slab for $\gamma = 0$, while for increasing γ it moves towards the end surface of the slab. As we mentioned earlier in Sec. III A, for $\omega = 10$ cm^{-1}, all the significant far-infrared Fourier components are nearly phase matched ($\Delta k_z l < \pi$). Therefore the curve for $\omega = 10$ cm^{-1} in Fig. 11 agrees fairly well with that described by $[1 - \exp(-\gamma l/2)]^2/(\gamma l/2)^2$ for the phase-matched plane-wave case. For $\omega = 100$ cm^{-1}, since not all the significant far-infrared Fourier components can be nearly phase matched, the reduction of far-infrared output with increasing absorption is slower and cannot be approximated by the phase-matched plane-wave form at small γ.

In some respects, the effects of γ for $\gamma l \geq 2$ can be simulated by an absorptionless crystal with a length $2\gamma^{-1}$. An increase of γ increases the phase-matching angle and broadens the phase-matched peak in the angular distribution of the far-infrared output. It also makes $(\Delta k_a)_{\text{opt}}$, the optimum axial phase mismatch for maximum total far-infrared

output, more negative. This latter effect is quite pronounced for $\omega = 100\ \mathrm{cm}^{-1}$ as shown in Fig. 12.

IV. COMPARISON WITH OTHER MODELS AND WITH CALCULATIONS OF SECOND-HARMONIC GENERATION

We now compare the results of our detailed calculations with those obtained from two simple models for the case where the optical walk-off effect is negligible. One is the Gaussian distribution (GD) model in which we assume a Gaussian profile for the nonlinear polarization at the difference frequency,

$$\vec{P}^{(2)}(\vec{r},t) = (\vec{\chi}^{(2)} : \vec{\mathcal{E}}_1 \vec{\mathcal{E}}_2^*) \times \exp[-2(x^2+y^2)/w^2 + i(k_1 - k_2)z - i\omega t] \tag{18}$$

in the crystal slab where the pump fields are given by

$$\vec{E}_j(\vec{r},t) = \vec{\mathcal{E}}_j \exp[-(x^2+y^2)/w^2 + ik_j z - i\omega_j t], \quad j = 1, 2 .$$

This is an extension of an earlier model used by Zernike and Berman[27] and Faries *et al.*[26] which assumes a uniform amplitude for $\vec{P}^{(2)}(\vec{r},t)$ throughout a cylinder with a finite radius. The other simple model is the usual plane wave model in which we assume that the geometric ray approximation is valid and that each beam can be described by a cylindrical pencil of rays with a single wave vector.

From the GD model, we obtain for the lossless case a total output power at ω of

$$\mathcal{P}_+^{\mathrm{GD}}(\omega) = \frac{\pi^2\omega^3 w^4}{4c^2} \left| \vec{\chi}^{(2)} : \vec{\mathcal{E}}_1 \vec{\mathcal{E}}_2^* \right|^2 l^2 \times \int_0^{\omega/c} dk_T (k_T/k_{oz}) \langle T(k_T) \rangle_\phi C(\Delta k_z) e^{-w^2 k_T^2/4}, \tag{19}$$

where $\langle T(k_T) \rangle_\phi$ is the far-infrared transmission factor averaged over the azimuthal angle ϕ with multiple reflections at the slab boundaries taken into account, and $C(\Delta k_z)$ describes the effect of phase mismatch. They are given by

$$\langle T(k_T) \rangle_\phi = \frac{1}{2(k_o + k_{oz})} \left(\frac{k_o (k_{oz} + n_o^2 k_z)^2}{k_{oz}^2 + n_o^4 k_z^2} + \frac{(k_{oz} + k_z)^2}{k_{oz}^2 + k_z^2} k_{oz} \right), \tag{20}$$

$$C(\Delta k_z) = \sin^2(\Delta k_z l/2)/(\Delta k_z l/2)^2 ,$$

with

$$\Delta k_z = n_o \omega/c + \Delta k_a - k_{oz} \quad \text{and} \quad \Delta k_a = k_1 - k_2 - n_o \omega/c .$$

The output powers at 100 and 10 cm^{-1} calculated from Eq. (19) as a function of w are shown in Figs. 13 and 14, respectively, in comparison with the results of Eq. (16) from our more exact calculations. At 100 cm^{-1}, the only perceptible difference between the two curves occurs at small beam sizes and amounts to 6% at $w = 13\ \mu\mathrm{m}$. At 10 cm^{-1},

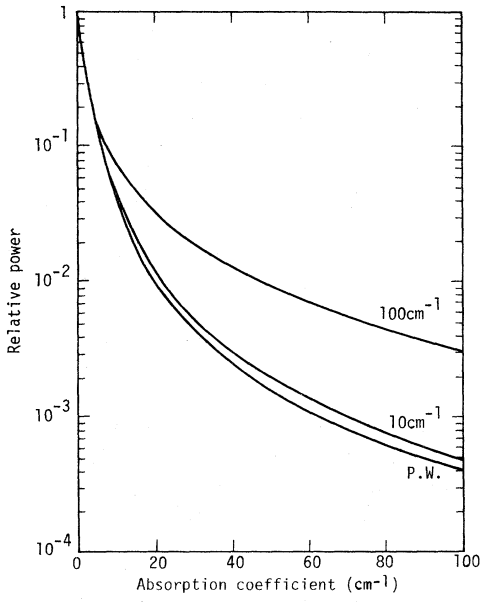

FIG. 11. $\mathcal{P}(\alpha)/\mathcal{P}(\alpha=0)$ vs α showing the reduction of output power due to far-infrared absorption. For each point on the curves for $\omega = 10$ and 100 cm^{-1}, $w = 25$ μm, an optimum value of Δk_a, and an optimum location of the focal plane were used in the calculation. A corresponding curve calculated from the plane-wave model is also shown for comparison.

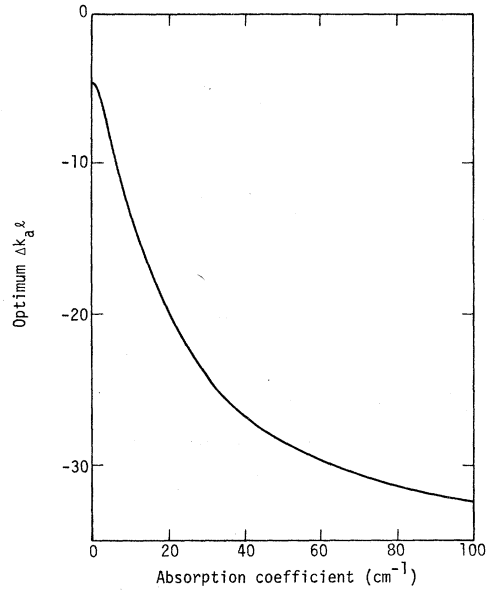

FIG. 12. Optimum values of $\Delta k_a l$ vs the absorption coefficient α for the case of Fig. 11 with $\omega = 100\ \mathrm{cm}^{-1}$ where Δk_a is the axial phase mismatch.

the two curves are virtually indistinguishable. Thus the GD model appears to be a very satisfactory approximation.

The output power from the plane-wave model without boundary conditions is given by

$$\mathcal{P}^{PW}(\omega)=\frac{\pi^2\omega^2 w^2}{2cn_o}\,|\chi^{(2)}:\vec{\mathcal{E}}_1\vec{\mathcal{E}}_2^{*}|^2 l^2\langle T(0)\rangle_\phi\,. \qquad (21)$$

The result calculated from Eq. (21) is also shown in Fig. 13. It is 20% higher than the correct value at $w=0.02$ cm. The deviation becomes much worse at smaller w and diverges as w approaches zero. This shows that the plane-wave model gives unacceptable results at small w because of its diffractionless approximation. With diffraction, the total far-infrared output power is decreased by total reflection of those Fourier components with large k_T and by phase mismatch [described by $C(\Delta k_z)$ in Eq. (19)] for other Fourier components.

The plane-wave calculation is, however, simple and does not require numerical integration. It is therefore preferred when one wants to crudely estimate the output power. We can make the estimate more exact by multiplying the calculated result by a correction factor. Comparison of Eqs.

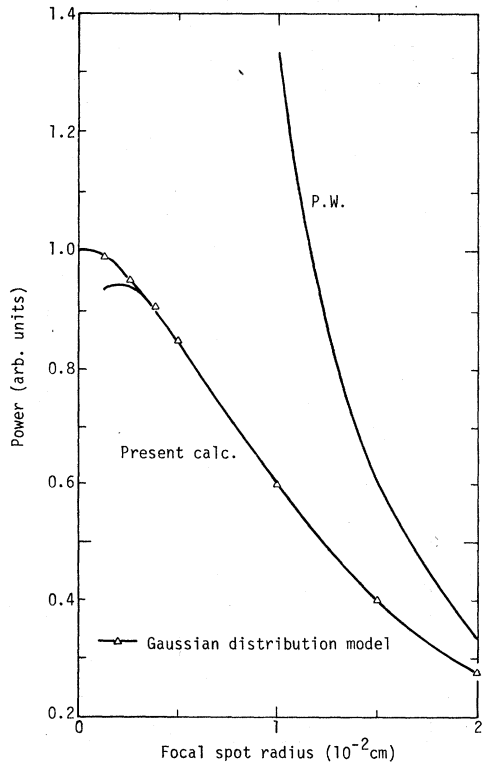

FIG. 13. Comparison of the results of the Gaussian distribution model, the plane-wave model, and our present calculation for $\omega=100$ cm^{-1}, $\alpha=0$, $\zeta=0$, and $l=1$ cm.

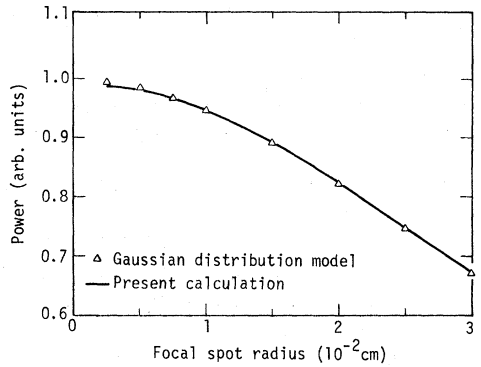

FIG. 14. Comparison of the results of the Gaussian distribution model and our present calculation for $\omega=10$ cm^{-1}, $\alpha=0$, $l=0$, and $l=1$ cm.

(19) and (21) shows that this correction factor is given by

$$F=\mathcal{P}^{GD}/\mathcal{P}^{PW},$$

$$=\frac{k_o w^2}{2\langle T(0)\rangle_\phi}\int_0^{\omega/c} dk_T\left(\frac{k_T}{k_{oz}}\right)\langle T(k_T)\rangle_\phi C(\Delta k_z)e^{-w^2k_T^2/4}. \qquad (22)$$

We approximate $\langle T(k_T)\rangle_\phi C(\Delta k_z)/k_{oz}$ in the integral by $\langle T(0)\rangle_\phi/k_o$ for $k_T<k_M$ and by 0 for[37] $k_T>k_M$ where k_M is defined as $k_M=[2\Delta k_c(n_o\omega/c-\Delta k_c/2]^{1/2}$ with Δk_c being the smaller of the two quantities $2\pi/l$ and $[n_o-(n_o^2-1)^{1/2}]\omega/c$. Physically, at $k_T=k_M$, $d\mathcal{P}/d\Omega$ either has dropped to half of its peak value or has been cut off by total reflection. The correction factor then becomes

$$F=1-e^{-k_M^2w^2/4}.$$

The output power calculated from $F\mathcal{P}^{PW}$ using Eqs. (21) and (23) is within 20% of the correct value.

We now discuss similarities and differences between difference-frequency generation (DGF) and second-harmonic generation (SHG). In both cases, each pump field $\vec{E}_i$ with finite beam radius has a distribution of Fourier components with wave vectors spreading effectively over an angle $2\delta_i$. The output of DFG or SHG from a nonlinear slab is significant only when part of these significant Fourier components within the angular spread $2\delta_i$ can satisfy the axial phase-matching condition $\Delta k_z=0$. As shown in Fig. 15, this happens for SHG only if $\Delta k_a^S\equiv 2k(\omega_1)-k(2\omega_1)\geq 0$ and $\Delta k_R^S\equiv 2k(\omega_1)(1-\cos\delta_1)\geq\Delta k_a^S$, and for DFG only if $\Delta k_a^D\equiv k_1-k_2-k(\omega)\leq 0$ and $\Delta k_R^D\equiv k(\omega)(1-\cos\delta)\geq-\Delta k_a^D$, where 2δ is the angular spread of the significant far-infrared Fourier components which can get out of the crystal slab. We emphasize that for an efficient nonlinear interaction we must have $\Delta k_a^S\leq 0$ for SHG and $\Delta k_a^D\geq 0$ for DFG.

The quantity Δk_R^S in SHG or Δk_R^D in DFG governs the qualitative behavior of the phase-matching curve $\mathcal{P}$ vs Δk_a. As we mentioned before, the output is most efficient when Δk_a^S (or $-\Delta k_a^D$) falls in the range between 0 and Δk_R^S (or Δk_R^D). Therefore if $\Delta k_R^S l$ (or $\Delta k_R^D l$) $\gg 2\pi$, then the phase-matching curve has a broad peak; it rises sharply to the peak around Δk_a^S (or Δk_a^D) = 0, then slopes downward as Δk_a^S (or Δk_a^D) increases from 0 to $\approx \Delta k_R^S$ (or Δk_R^D), and finally in the case of DFG falls rapidly at a certain Δk_a^D value because of the cutoff due to total reflection at the boundaries. Examples are shown in Fig. 4 for DFG with $\Delta k_R^D l = 80$ and in Fig. 16 for SHG with $\Delta k_R^S l = 100$.[31] Such a phase-matching curve is characteristic of SHG with strong focusing of the pump beam. In DFG it occurs when the pump beams are more weakly focused because of large far-infrared diffraction. When $\Delta k_R^S l$ (or Δk_R^D) $\lesssim 2\pi$ the range of Δk_a^S (or Δk_a^D) for efficient output is much narrower, and the phase-matching curve now shows a central peak and secondary maxima and minima, resembling the well-known plane-wave phase-matching curve described by $\sin^2(\Delta kl/2)/(\Delta kl/2)^2$. Examples are shown in Fig. 5 for DFG at 100 cm^{-1} with $\Delta k_R^D l = 4$, in Fig. 9 for DFG at 10 cm^{-1} with $\Delta k_R^D l = 8$, and in Fig. 17 for SHG with $\Delta k_R^S l = 5.68$. All these curves are, however, slightly asymmetric with a small shoulder on one side. This is because for $\Delta k_a^S l < 0$ (or $\Delta k_a^D > 0$), the phase-matching condition $\Delta k_z = 0$ is not satisfied for any of the Fourier components.

There are several minor differences between the SHG and DFG phase-matching functions. For $\Delta k_R^S l$ (or $\Delta k_R^D l$) $\gg 2\pi$, the phase-matching curve for DFG, as shown in Fig. 4, has a sharp drop around the value of Δk_a^D where significant Fourier components of the far-infrared output begin to be

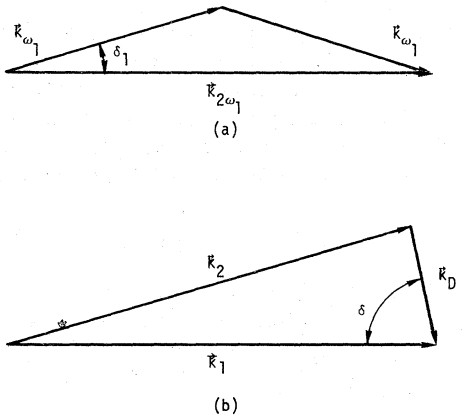

FIG. 15. Phase-matched wave-vector diagrams for (a) second-harmonic generation and (b) difference-frequency generation.

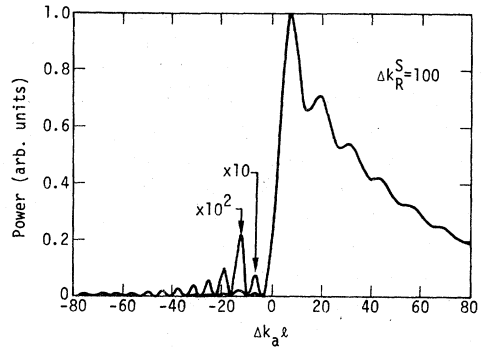

FIG. 16. Second-harmonic power output as a function of $\Delta k_a l$ when $\Delta k_R^S l = 100$. [After Boyd and Kleinman, J. Appl. Phys. 39, 3597 (1968)].

totally reflected at the boundaries. In SHG, however, total reflection is never important and therefore as shown in Fig. 16, no sudden drop of the output power occurs as Δk_a^D increases. Because of the weaker diffraction effect, the phase-matching curve for SHG has, in general, more pronounced fine structure than that for DFG.

V. CONCLUSION

We have developed here the theory of far-infrared generation by optical mixing in a nonlinear medium, using an extension of a formalism developed earlier for second-harmonic generation by focused laser beams. The theory takes into account the effects of focusing, diffraction, and double refraction of the pumped beams and the effects of diffraction, absorption, and reflections at the boundaries of the far-infrared output beam. Numerical calculations showing these effects are presented. Both the total power output and its angular distribution are calculated.

We have found that focusing of the pump beams

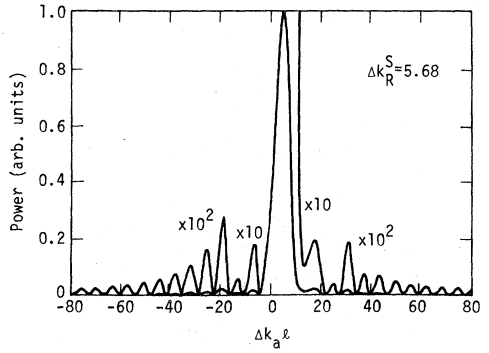

FIG. 17. Second-harmonic power output as a function of $\Delta k_a l$ when $\Delta k_R^S l = 5.68$. (After Boyd and Kleinman *op.cit.*)

can greatly enhance the far-infrared output. In a crystal of 1 cm length, the optimum focal spot radius is roughly equal to or smaller than the far-infrared wavelength for output frequencies less than 100 cm^{-1}. The walkoff effect of the pump beams in birefringent crystals does not reduce the output by more than a factor of 2. Far-infrared absorption and boundary reflections are, however, extremely important. The former is often the factor which limits the output power.

We show that the usual plane-wave model which neglects the effects of far-infrared diffraction and boundary reflections does not give a correct description of the far-infrared output, especially for tightly focused pump beams. A simple model treating the nonlinear polarization as a constant-$1/e$-radius Gaussian distribution of radiating dipoles is, however, a good approximation to the real picture. We also compare our results with those of second-harmonic generation and notice a great deal of similarities. Most of the differences can be ascribed to the boundary effects, including total reflection, which are more important in the case of far-infrared generation.

ACKNOWLEDGMENTS

This research was supported by the U. S. Energy Research and Development Administration. One of the authors (J.R.M.) would like to thank the Lawrence Livermore Laboratory for providing computer time and R. L. Pexton for providing complex error function and numerical integration subroutines. The other (Y.R.S.) is indebted to the Miller Institute of University of California for a research professorship.

APPENDIX A

The extraordinary ray assumed in Sec. II A actually has the form

$$\vec{E}_2(\vec{r},t)=\frac{\mathcal{E}_2\hat{e}_2(1+\xi_\Delta^2)^{1/2}}{[(1+i\xi_{2x})(1+i\xi_{2y})]^{1/2}} \times\exp\left(-\frac{(x-\zeta_2 z)^2}{w_2^2(1+i\xi_{2x})}-\frac{y^2}{w_2^2(1+i\xi_{2y})}\right) \times\exp[i(k_2z-\omega_2t)], \tag{A1}$$

where

$$\xi_\Delta=(z_{0,2x}-z_{0,2y})n_2^4/\{k_2w_2^2n_{em,2}^2(n_2^2+n_{o,2}^2)\},$$
$$\xi_{ex}=2(z-z_{0,2x})[n_2^4/\{k_2w_2^2n_{em,2}^2n_{o,2}^2\}],$$
$$\xi_{ey}=2(z-z_{0,2y})[n_2^2/\{k_2w_2^2n_{em,2}^2\}],$$

with $\hat{e}_2$ being a unit vector parallel to the electric field of the e ray for a normally incident laser beam and the remaining parameters are as defined for Eq. (1). This expression with $z_{0,2x}=z_{0,2y}$ is essentially the same as the one given in Appendix I of Ref. 31, but there the factors in the square brackets in the definition of ξ_{2x} and ξ_{2y} were approximated by 1.

The nonlinear polarization $\vec{P}^{(2)}(\vec{r},\omega)$ is obtained from Eq. (2) using the expressions of $\vec{E}_1$ in Eq. (1) and $\vec{E}_2$ in Eq. (A1). The transverse Fourier transform of $\vec{P}^{(2)}(\vec{r},\omega)$ gives $\vec{P}^{(2)}(\vec{k}_T,z)$. To obtain the expression of $\vec{P}^{(2)}(\vec{k}_T,z)$ in Eq. (3), we made the following simplifying assumptions. First, we assumed $w_1=w_2=w$. Second, we assumed a common focus for the two beams, $z_{0,1}=z_{0,2x}=z_{0,2y}=z_0$. Finally, we assumed $\xi_1-\xi_{2x}\simeq\xi_1-\xi_{2y}=0$. This last assumption is reasonable as long as $3|\xi_1-\xi_{2x}|, 3|\xi_1-\xi_{2y}|\ll\pi/2$. In our calculations, the largest value of $3|\xi_1-\xi_{2x}|$ or $3|\xi_1-\xi_{2y}|$ is 1 for the case of $\omega=10$ cm^{-1}, $w=25$ μm and $\zeta=-0.02$. For all the other cases, $3|\xi_1-\xi_{2x}|$ or $3|\xi_1-\xi_{2y}|$ is much smaller than 1.

APPENDIX B

To derive Eq. (6), we first Fourier transform Eq. (4) and obtain

$$[\vec{k}\vec{k}-k^2\vec{1}+\omega^2\vec{\epsilon}/c^2]\cdot\vec{E}(\vec{k})=-4\pi(\omega^2/c^2)\vec{P}^{(2)}(\vec{k}),$$
$$\vec{k}\cdot\vec{\epsilon}\cdot\vec{E}(\vec{k})=-4\pi\vec{k}\cdot\vec{P}^{(2)}(\vec{k}). \tag{B1}$$

The particular solution of Eq. (B1) can be written in the form

$$\vec{E}^p(\vec{k})=\vec{S}(\vec{k})\cdot\vec{P}^{(2)}(\vec{k}).$$

From the inverse transform on k_z, we then have

$$\vec{E}^p(\vec{k}_T,z)=\frac{1}{2\pi}\int_{-\infty}^{\infty}dk_z\int_{-\infty}^{\infty}dz'e^{ik_z(z-z')}\vec{S}(\vec{k})\cdot\vec{P}^{(2)}(\vec{k}_T,z'). \tag{B2}$$

A straightforward, but tedious, application of the residue theorem finally leads to Eq. (6).

We also notice that Eqs. (6) and (7) are not the results of slowly varying envelope approximation. This is in fact generally true for the solution of optical mixing in the parametric approximation. For example, consider the simple case where the nonlinear process can be described by the wave equation

$$(\partial^2/\partial z^2+k_o^2)E(z)=4\pi(\omega^2/c^2)P^{\mathrm{NL}}(z), \tag{B3}$$

where $P^{\mathrm{NL}}(z)\neq0$ only if $0\leq z\leq l$. Then, in the region $0\leq z\leq l$, the solution of the equation is

$$E(z)=\frac{2\pi\omega^2}{ik_oc^2}\left(\int_0^z P^{\mathrm{NL}}(z')e^{ik_o(z-z')}dz' + \int_z^l P^{\mathrm{NL}}(z')e^{-ik_o(z-z')}dz'\right). \tag{B4}$$

No slowly varying envelope approximation was

made in the derivation. In fact, one can easily show that with the complete expression of $E(z)$ in Eq. (B4), the terms $\partial^2|E(z)|/\partial z^2$ and $2k_0\partial|E(z)|/\partial z$ are generally comparable in magnitude. The usual slowly varying envelope approximation is actually equivalent to neglecting waves propagating in the opposite direction.

---

*Present address: Theoretical Division, Lawrence Livermore Laboratory, P.O. Box 808, Livermore, Calif. 94550.

[1]For a recent review of nonlinear optical processes for generating far-infrared radiation which covers both applicable DFG experiments and basic theory see Y. R. Shen, Prog. Quantum Electron. 4, 207 (1976).
[2]K. H. Yang, J. R. Morris, P. L. Richards, and Y. R. Shen, Appl. Phys. Lett. 23, 669 (1973).
[3]D. H. Auston, A. M. Glass, and P. LeFur, Appl. Phys. Lett. 23, 47 (1973).
[4]F. Zernike, Bull. Am. Phys. Soc. 12, 687 (1967).
[5]T. Y. Chang, N. VanTran, and C. K. N. Patel, Appl. Phys. Lett. 13, 357 (1968).
[6]N. VanTran and C. K. N. Patel, Phys. Rev. Lett. 22, 463 (1969).
[7]C. K. N. Patel and N. V. Tran, Appl. Phys. Lett. 15, 189 (1969).
[8]T. J. Bridges and T. Y. Chan, Phys. Rev. Lett. 22, 811 (1969).
[9]F. Zernike, Phys. Rev. Lett. 22, 931 (1969).
[10]N. VanTran, A. R. Strnad, A. M. Jean-Louis, and G. Duraffourg, in *The Physics of Semimetals and Narrow Gap Semiconductors*, edited by D. L. Carter and R. T. Bates, (Pergamon, New York, 1971), p. 231.
[11]V. T. Nguyen and T. J. Bridges, Phys. Rev. Lett. 29, 359 (1972).
[12]T. J. Bridges and A. R. Strnad, Appl. Phys. Lett. 20, 382 (1972).
[13]G. D. Boyd, T. J. Bridges, C. K. N. Patel, and E. Buelher, Appl. Phys. Lett. 21, 553 (1972).
[14]R. L. Aggarwal, B. Lax, and G. Favrot, Appl. Phys. Lett. 22, 329 (1973).
[15]B. Lax, R. L. Aggarwal, and G. Favrot, Appl. Phys. Lett. 23, 679 (1973).
[16]N. Lee, R. L. Aggarwal, and B. Lax, Opt. Commun. 11, 339 (1974).
[17]T. J. Bridges and V. T. Nguyen, Appl. Phys. Lett. 23, 107 (1973).
[18]V. T. Nguyen and T. J. Bridges, in *Laser Spectroscopy*, edited by R. G. Brewer and A. Mooradian (Plenum, New York, 1974), pp. 513–521.
[19]T. J. Brignall, R. A. Wood, C. R. Pidgeon, and B. S. Wherrett, Opt. Commun. 12, 17 (1974).
[20]V. T. Nguyen and T. J. Bridges, Appl. Phys. Lett. 26, 452 (1975).
[21]T. Yajima and K. Inoue, IEEE J. Quantum Electron. 5, 140 (1969).
[22]F. deMartini, Phys. Lett. A 30, 547 (1969).
[23]F. deMartini, Phys. Rev. B 4, 4556 (1971).
[24]D. W. Faries, P. L. Richards, Y. R. Shen, and K. H. Yang, Phys. Rev. A 3, 2148 (1971).
[25]T. L. Brown and P. A. Wolff, Phys. Rev. Lett. 29, 362 (1972).
[26]D. W. Faries, K. A. Gehring, P. L. Richards, and Y. R. Shen, Phys. Rev. 180, 363 (1969).
[27]F. Zernike, Jr. and P. R. Berman, Phys. Rev. Lett. 15, 999 (1965).
[28]D. W. Faries, Ph.D. Thesis, University of California, Berkeley (1969).
[29]J. E. Bjorkholm, Phys. Rev. 142, 126 (1966).
[30]D. A. Kleinman, A. Ashkin, and G. D. Boyd, Phys. Rev. 145, 338 (1966).
[31]G. D. Boyd and D. A. Kleinman, J. Appl. Phys. 39, 3597 (1968).
[32]See, for example, P. C. Clemmow, *The Plane Wave Spectrum Representation of Electromagnetic Fields* (Pergamon, New York, 1966); and E. Lalor, J. Math. Phys. 13, 437 (1972) for discussions of this method.
[33]Optical rectification was first reported by M. Bass, P. A. Franken, J. F. Ward, and G. Weinreich, Phys. Rev. Lett. 9, 446 (1962). For a discussion of the theory of optical rectification see M. Bass, P. A. Franken, and J. F. Ward, Phys. Rev. 138A, 534 (1965).
[34]N. Bloembergen, *Non-linear Optics* (Benjamin, New York, 1965), pp. 74–81.
[35]M. Berek, Z. Kristallog. 76, 396 (1931). The fields in this work are magnetic fields (in spite of notation which suggests they are electric fields) because the Brewster's angle occurs for the "senkrecht" or perpendicular polarization. After these equations are rewritten in terms of electric fields, the "one-ray" coefficients are the elements of our $\tilde{A}$ and $\tilde{B}$ matrices. For an English translation with some typographical errors, see G. N. Ramachandran and S. Ramasesham, in *Handbuch der Physik*, edited by S. Flugge, Vol. XXV/1 (Springer-Verlag, Berlin, 1961), pp. 117–119.
[36]K. Miyamoto and E. Wolf, J. Opt. Soc. Am. 52, 615 (1962). Note that their definition of the Fourier transform is smaller than our definition by a factor of $1/2\pi$.
[37]For tightly focused exp $[-\frac{1}{4}w^2k_T^2] \cong 1$ when $k_T < \omega/c$, and this factor can be pulled outside the integral in Eq. (19) along with $\langle T'(k_T)\rangle_\phi$. Then, the remaining integral is $\int_0^{\omega/c} k_T dk_T C(\Delta k_z)/k_{0z}$ which has the value $\simeq \pi/l$ for thick crystals or high far-infrared frequencies and the value $\simeq(\omega/2c)\{n(\omega)-[n^2(\omega)-1]^{1/2}\}$ for thin crystals or low far-infrared frequencies.